ACS MATERIALS LETTERS

www.acsmaterialsletters.org

Omni-Directional Ultrasonic Powering via Platonic Solid Receiver for mm-Scale Implantable Devices

Sayemul Islam, Eungyoul Oh, Chaerin Jun, Jungkwun Kim, Won Seok Chang,* Seunghyun Song,* and Albert Kim*

Cite This: *ACS Materials Lett.* 2023, 5, 1876–1885

Read Online

ACCESS | Metrics & More | Article Recommendations | Supporting Information

ABSTRACT: **Despite the recent advancements in implantable microdevices, providing sufficient electrical power to deeply seated microsystems has remained challenging due to the small dimension of the system, limiting the total storable energy. Ultrasound powering, where a portion of the externally induced ultrasonic wave is converted to electrical power by a small receiver, has been explored as an attractive source of power, especially for deeply seated implantable microdevices. While all other components have been advanced and miniaturized, the ultrasonic receiver is still a slab of bulk piezoelectric materials, e.g., diced PZT (lead zirconate titanate). Such a rectangular or disc shape is not an ideal form factor for wireless ultrasonic power transfer due to many challenges, particularly angular sensitivity with respect to an incoming ultrasonic wave. In this paper, we present the first demonstration of omnidirectional ultrasonic powering enabled by the high geometrical symmetry of three-dimensional polyhedral shapes. Based on our 3D printing technique of lead-free piezoelectric barium titanate ceramic, we designed highly symmetric, miniaturized, regular polyhedra, known as Platonic solids (i.e., cube, octahedron, dodecahedron), as well as a sphere. For each geometry, we investigate the effect of axial and radial piezoelectric poling, output power levels, efficiency, and angular sensitivity while the surface areas are the same. Across all the geometric shapes, radially poled Platonic solid receivers produce at least 1 order of magnitude larger electrical power density compared to diced PZT. Further, we observed that the higher the order of Platonic solid, the more excellent power transfer efficiency and omnidirectionality. The 3D printability of the Platonic solid also allows for customizable packaging, which we implemented as an implantable light source. Overall, the proposed ultrasonic powering scheme warrants a revolutionary solution for implantable biomedical devices.**

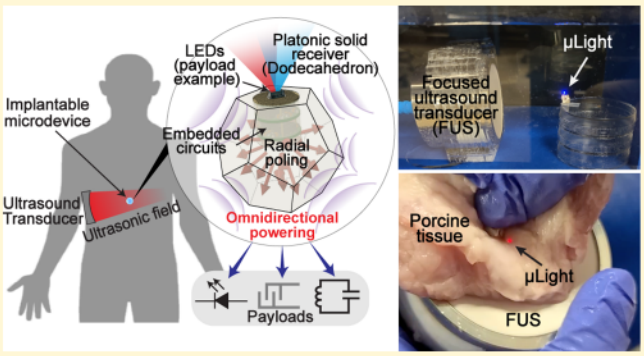

Since the clinical success of the pacemaker in the 1960s,[1,2] subsequent decades have witnessed abundant new implantable medical devices entering the clinics. Leveraging advances in nano/microelectromechanical systems (N/MEMS), integrated circuits, wireless communication, and battery technologies,[3−6] implantable medical devices (IMDs) opened a new era of modern healthcare. For example, the modern pacemaker has a reduced weight and can be fabricated to a couple of centimeters in length.[7] A coin-sized neural implant for the brain-machine interface (equipped with thousands of microelectrodes, a processor, and often wireless communication) is another noteworthy approach.[8] Such emerging implantable devices indeed enable next-generation therapy, especially by leveraging the ability to localize treatments.

While all other components of the IMDs have been significantly miniaturized, the rate of battery size reduction is gradual. It is because the battery size dictates the device's lifetime, and this means that a patient needs to undergo another painful surgery for battery replacement. Thus, a principle for the extended operation of these IMDs would be a sufficient and dependable power supply. Remarkable advances in the energy source for IMDs in this timeline would be the

Received: February 4, 2023
Accepted: May 15, 2023
Published: May 31, 2023

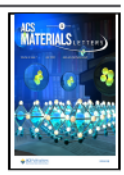

lithium-ion battery and inductive powering.[9,10] Wilson Greatbatch, a pioneering entrepreneur, was the first to implement lithium-ion batteries in his invention, the pacemaker.[11,12] It dramatically increased the pacemaker's lifetime, resulting in a reduction in the number of battery replacement surgeries. Inductive powering is an alternative energy source for IMDs that cannot employ a battery, primarily due to extensive power utilization (e.g., cochlear implants)[13] or insubstantial anatomical space (e.g., intraocular implants).[14] Over the last 50 years, inductive powering has dominated the wireless powering of many implantable devices. However, some practical challenges exist, such as tissue heating, limited operation distances, sensitive angular misalignment, and difficulties in fabricating small coils that have adequate quality factors.

Ultrasonic powering was introduced as a promising resolution of the above-mentioned shortcomings, particularly for millimeter-scale implantable devices.[15−20] Using a piezoelectric receiver, ultrasonic waves propagating through the body are converted into electrical energy. The resulting electrical energy then powers various vital sensing, stimulation, and more.[6,21−23] Compared to inductive powering, ultrasonic powering presents numerous advantages, including a long operation distance, high efficiency, and a small receiver (millimeter-scale). For example, it is reported that a 2 mm receiver could achieve an order of magnitude higher power transfer efficiency compared to inductive powering at 10 cm from the transmitter (0.02% vs 0.00002%).[24]

Despite the advantages, ultrasonic powering is still challenged by angular misalignment sensitivity. Ideally, the piezoelectric receiver face should be orthogonal to the incident ultrasonic waves to achieve the highest energy conversion efficiency (the piezoelectric poling direction and the ultrasonic wave must be parallel). However, commonly used form factors for piezoelectric receivers are cuboids or discs, which can be quite sensitive to angular misalignment. While these piezoelectric receivers are poled between two parallel planes of electrodes, inhomogeneous acoustic media deflect the incident ultrasonic waves within the path. Also, the small implants often move around, shift, and rotate within the body, resulting in significant angular misalignment. In our previous study, we found that a symmetrical cuboidal receiver could reduce such angular misalignment sensitivity. The symmetry allows the deformation in the lateral direction to couple with the poling direction via the Poisson ratio, inducing synergistic power generation.[15] However, geometric limitations, i.e., vertices and edges of the cuboidal receiver, still exhibited significant power loss when the angular alignment was off. This, paired with the fact that a small receiver is difficult to align with the transmitter, makes stable powering of deep tissue implantation exceptionally challenging. Additionally, many ultrasonic powering materials reported in the literature use lead zirconate titanate (PZT),[16,17] which raises a significant safety concern due to the risk of lead poisoning.

Here, we present a 3D printable, lead-free, barium titanate ($BaTiO_3$) for omnidirectional ultrasonic powering by adopting a Platonic solids design, i.e., a highly symmetrical polyhedron with a regular polygon as the faces. In addition, we introduce radial poling to increase the symmetry even further. Owing to such geometric symmetry and radial poling, the Platonic solid ultrasonic receivers increase the probability of aligning the incident waves and poling vector at any given angle, resulting in improved power transfer efficiency. Moreover, the Platonic solids receivers could be engineered for the seamless packaging of various vital payloads (e.g., electrical stimulation, electrochemical reaction,[18] or an LC (inductor-capacitor) resonator for wireless sensing[25]). For example, we demonstrated an implantable light source using the Platonic solid receiver by pairing it with light-emitting diodes (LEDs).[19] The Platonic solid receivers were experimentally investigated for angular, distal, and intensity responses, as well as the total power output. We also demonstrated ultrasonic powering and packaging electronics using a Platonic solid receiver for an implantable light source.[19] This implantable light source can transform existing Photodynamic therapy (PDT),[19] Photobiomodulation (PBM),[26] or optogenetics[27] to treat deeply seated infirmities.

Platonic solids are convex polyhedra with faces of an identical regular polygon.[28] The five Platonic solids are the tetrahedron, cube, octahedron, dodecahedron, and icosahedron. The tetrahedron, octahedron, and icosahedron consist of 4, 8, and 20 triangular faces, respectively. The cube is the only Platonic solid with six square faces. The dodecahedron has 12 pentagonal faces. These remarkably symmetrical shapes enable the ultrasonic receiver's three-dimensional structural diversity to be tailored for greater angular misalignment insensitivity. With the highly symmetric shape, tailoring such three-dimensional structural diversity in the ultrasonic receiver can enhance the ultrasonic power efficiency. The higher degree Platonic solids, such as the octahedron, dodecahedron, and icosahedron, increase the probability of aligning the incident ultrasonic waves with the poling direction by a factor of their number of faces (8, 12, and 20 faces, respectively). When accounting for all projected faces of higher-degree Platonic solids seen by the incoming ultrasonic waves, it can sustain a relatively consistent effective receiving area throughout any angular misalignment. Supplementary Figure 1 shows the effective area as a function of angular rotation, which is repeated periodically due to symmetry. For instance, the effective receiving area repeats every 18° for the dodecahedron and every 30° for the octahedron. In the case of a cube, the effective area repeats much less frequently at every 45°. The sphere has an indefinite periodicity as it is the highest-degree polyhedron.

To test our hypothesis of geometric effects enabling omnidirectional powering, we chose four Platonic solids: cube, octahedron, dodecahedron, and sphere. The tetrahedron was excluded since its periodicity is less than a cube, i.e., a typical form factor used in IMDs.[6,15] We scaled the dimensions of each Platonic solid to have the same overall surface area so that the geometry would primarily determine the power output. The Platonic solids' structure and size are shown in Table 1. The radius of the sphere was set to 3.5 mm, the edge lengths of the cube, octahedron, and dodecahedron to 5.07,

Table 1. Summary of Platonic Solid Receivers Design

Platonic solid	Number of faces	Surface area formula	Dimension (mm)[a]	Overall surface area (mm^2)
Cube	6	$6a^2$	a = 5.07	152.22
Octahedron	8	$2\sqrt{3}\,a^2$	a = 6.67	154.14
Dodecahedron	12	$3\sqrt{25+10\sqrt{5}}\,a^2$	a = 2.73	153.87
Sphere	Inf	$4\pi r^2$	r = 3.5	153.94

[a] a = length of edge, r = radius

https://doi.org/10.1021/acsmaterialslett.3c00121
ACS Materials Lett. 2023, 5, 1876−1885

6.67, and 2.73 mm, respectively, and thus, the total surface area of each solid was equalized to 154.04 ± 0.164 mm^2.

We create the Platonic solid ultrasonic receiver using barium titanate ($BaTiO_3$) due to its processing flexibility, biocompatibility, and good mechanical and piezoelectric properties (Table 2). The fabrication of Platonic solid receivers was adopted from our previous work[31] (Figure 1b) (see Experimental Section). As seen in scanning electron microscope images (SEM; FEI Quanta FEG-250) (Figure 1c,d), we observed the morphological change from $BaTiO_3$ nanoparticles fused into larger micron-sized grains after the sintering (i.e., postprocessing). The crystal structures and orientation of the fabricated $BaTiO_3$ Platonic solids (Figure 1e) were obtained from X-ray diffraction (XRD; Bruker D8 Advance powder XRD, Cu–Kα radiation (λ = 1.5418 Å, 40 kV, 40 mA) in reflection mode). The diffraction peaks were consistent with the literature.[32,33] The splitting peaks at 2θ near 22° and 45° confirmed the tetragonal phase of $BaTiO_3$. We could also observe the peak ratios of (001)/(100) and (002)/(200) enhanced after poling, which indicate the aligned piezoelectric domains with the poling direction (001).

Although the high rotational symmetry allows a consistent effective receiving surface that aligns with the incident ultrasonic waves, this advantage can be diminished by a single-axis piezoelectric poling direction. Therefore, we introduced a new poling direction, radial poling (Figure 2a,b, compare axial and radial), to take full advantage of the high symmetry of the Platonic solids receivers. The axial poling (traditional poling direction) was completed through two

Table 2. Summary of $BaTiO_3$ Material Properties[29,30]

Properties	Value
Density (g/cm^3)	5.80
Young's modulus (GPa)	67
ε'	1680
k_t	0.26
d_{33} (pC/N)	160–350
g_{33} (Vm/N)	11.4
Acoustic velocity (m/s)	1790

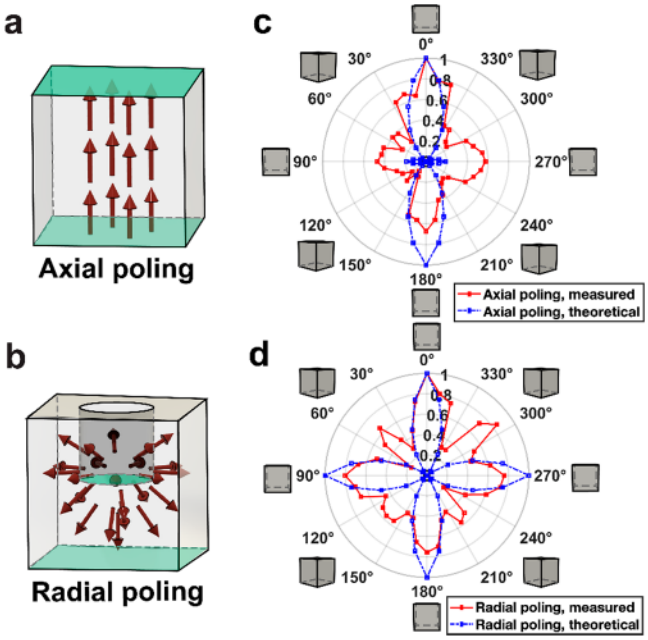

Figure 2. Effect of the poling directions: An illustration of (a) an axial (traditional) and (b) a radial poling. (c) Experimentally measured and simulated voltage output response of an axially poled cube and (d) a radially poled cube; poling in the radial direction improves the average voltage and d_{33} response.

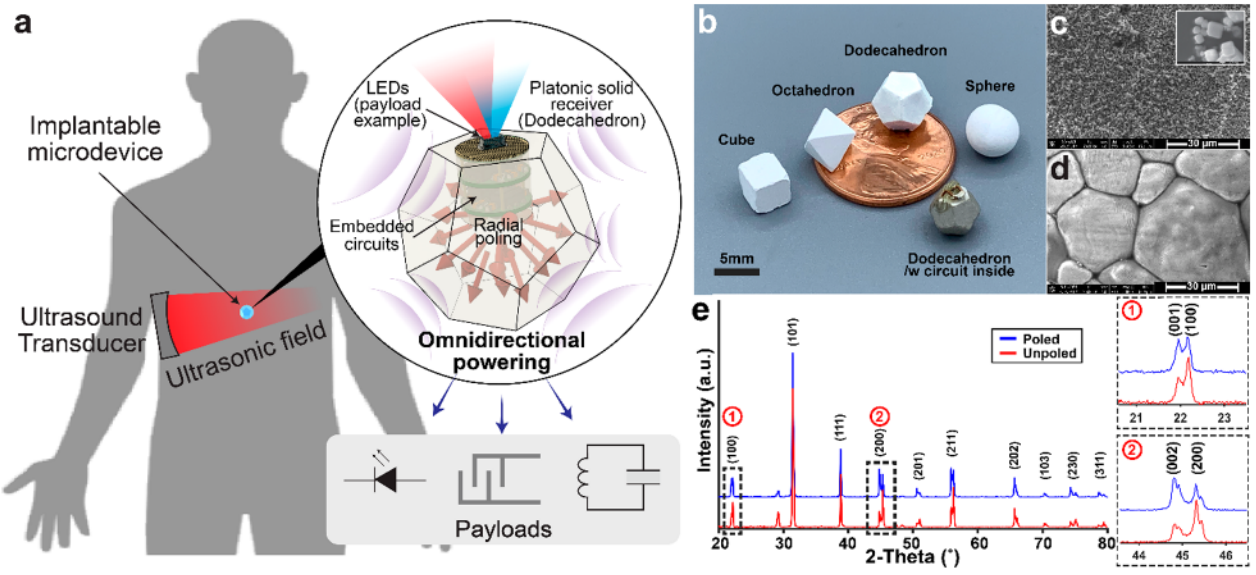

Figure 1. (a) Omnidirectional ultrasonic powering for deeply seated miniature implants: Platonic solids (dodecahedron is shown as an example) capture a portion of externally introduced ultrasonic waves with a greater number of faces orthogonal to the incident waves and convert them to electrical power to energize implantable devices with various payloads (e.g., sensor, stimulator, wireless resonator). The Platonic solid can also be customized to provide the inner space for seamless packaging of electronics (i.e., a power recovery circuit, rectifier, or other loads). (b) Fabricated Platonic solid receivers: cube, octahedron, dodecahedron, and sphere. The dodecahedron with a circuit inside is also shown in the bottom right corner. (c) SEM pictures are shown after binding and (d) sintering. (e) X-ray diffraction patterns: splitting peaks at 22° (100/001) and 45° (200/002) indicate piezoelectricity due to poling.

https://doi.org/10.1021/acsmaterialslett.3c00121
ACS Materials Lett. 2023, 5, 1876–1885

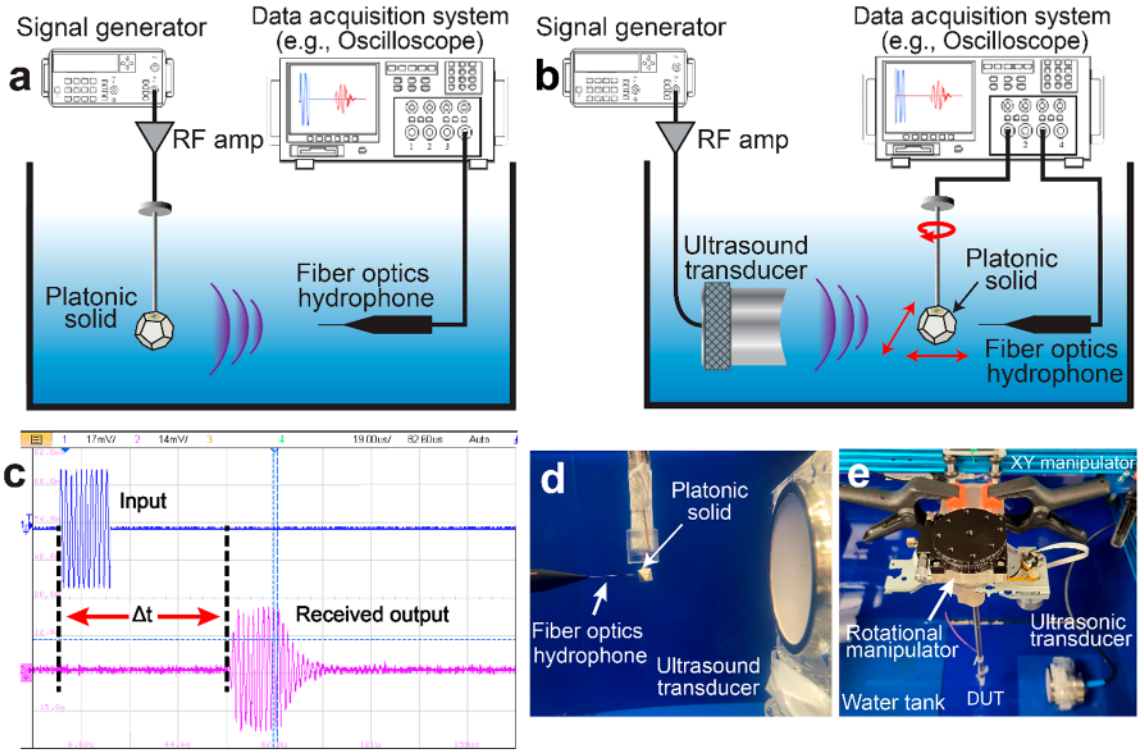

Figure 3. Ultrasonic powering experimental setups for (a) resonance frequency study, (b) transducer offset, distance, and rotational symmetry study. (c) Example of an input and received output signal: the input is the ultrasonic wave generator in the electrical domain. The received signal is the electrical energy received from the Platonic solids. A picture of the experimental setup: (d) resonant frequency study: a fiber-optic hydrophone is placed directly next to the Platonic solid to measure acoustic intensity sensitivity, (e) transducer offset, distance, and rotational symmetry study: a custom XY and rotational manipulator platform was used for the measurements.

parallel faces. Figure 2c shows the corresponding voltage response for axial poling. To enable the radial poling, we sacrificed one face of the Platonic solid and hollowed it out up to the center. The poling was done by applying a high electrical field (>1 kV/mm) between all outer faces and the center in a silicone oil bath heated above 120 °C for over 4 h. Therefore, the poling direction was radially outward, corresponding to the radial direction in spherical coordinates, from the center to the outer surface of the Platonic solids (Figure 2d). Comparing axial and radial poling in terms of the actual voltage outputs under the same ultrasound intensity, the axially poled cube produced 0.54 V on average (for a full 360° rotation), while the radially poled cube produced 0.75 V on average (for a full 360° rotation), which was a 39% improvement.

Neglecting the shear components, the induced charge density from a single plane whose normal vector faces the incoming ultrasound at an angle (θ) can be calculated using the piezoelectric coefficients d_{33} and d_{31} (Supplementary Figure 2 shows the theoretical calculation for angular responses). Subsequently, the output can be estimated by adding the accumulated charges from all surfaces.

$$Q = \sum A_0 T \cos\theta_i d_{eff_i} \tag{1}$$

$$d_{eff_i} = d_{33}|\cos(180 - (\alpha_i - \theta_i))| + d_{31}|\sin(180 - (\alpha_i - \theta_i))| \tag{2}$$

where A_0 denotes an effective area, α is the poling direction, determined by the geometry of the Platonic solids, T is the mechanical stress due to the incident ultrasonic wave, and d_{eff} is the effective piezoelectric coefficient due to the geometric effect of the Platonic solids.

The computational model was experimentally validated using identical cubical $BaTiO_3$ piezoelectric receivers but in two different poling directions: axial vs radial. The voltage outputs were measured while they were exposed to ultrasonic waves at their resonant frequencies. The resonant frequencies were mainly determined by the geometry, which was experimentally determined and validated via COMSOL simulation, shown in Supplementary Figure 3. The Platonic solids without cylindrical void (for axial poling) showed an average resonant frequency of 382.5 ± 58.5 kHz ($f_{r,axial,\ Cube}$ = 310 kHz, $f_{r,axial,\ Octahedron}$ = 400 kHz, $f_{r,axial,\ Dodecahedron}$ = 370 kHz, $f_{r,axial,\ Sphere}$ = 450 kHz). The Platonic solids with cylindrical voids (for radial poling) shifted these resonant frequencies to a higher region of 497.5 ± 9.6 kHz due to higher-order vibration modes ($f_{r,radial,\ Cube}$ = 500 kHz, $f_{r,radial,\ Octahedron}$ = 490 kHz, $f_{r,radial,\ Dodecahedron}$ = 510 kHz, $f_{r,radial,\ Sphere}$ = 490 kHz).

When the ultrasonic wave and the electrode sides (0° and 180°) were orthogonal, the receiver generated the highest open circuit voltage (V_{OC}) for both axial and radial poling. The distinction appeared on the lateral sides, i.e., 90° and 270°, where the highest V_{OC} was repeated for the radial poling. In the computation model, the V_{OC} showed a stiff decrease at 45°, 135°, 225°, and 315° (Figure 2c,d). At these angles, the vertex of the receiver was facing the incoming ultrasonic waves and scattered them out. The experimental results, however, showed a slight difference. The scattered waves still vibrate the receiver in the longitudinal direction (d_{31}), which is about half of d_{33}. This was also more resilient for the radially poled transducer, demonstrating a significant enhancement in omnidirectionality.

https://doi.org/10.1021/acsmaterialslett.3c00121
ACS Materials Lett. 2023, 5, 1876−1885

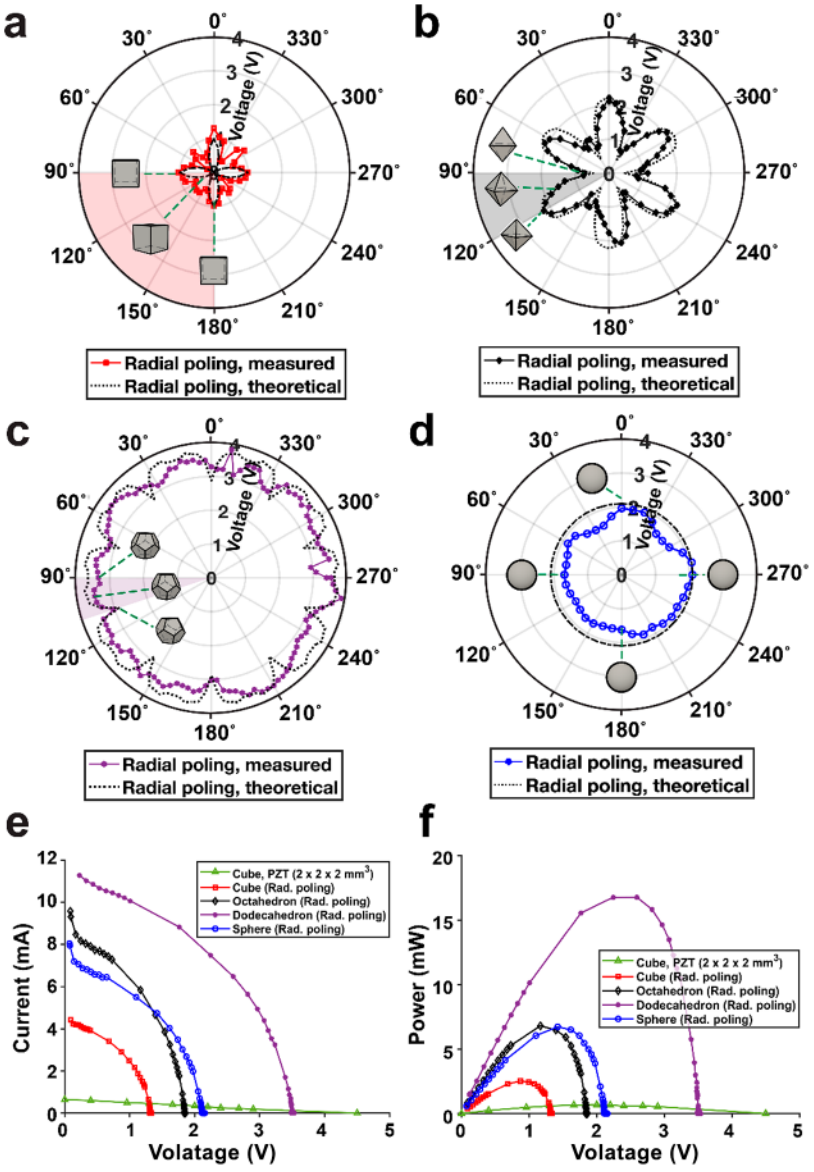

Figure 4. Electrical response due to symmetric Platonic solids designs and radial poling: (a) cube (capacitance = 276.2 pF), (b) octahedron (capacitance = 207.0 pF), (c) dodecahedron (capacitance = 329.31 pF), and (d) sphere (capacitance = 284.29 pF). The measured (e) current−voltage (IV) characteristics with variable resistive loads and (f) power density.

As seen in the cubical receiver, the voltage output (V_{OC}) was repeated periodically as the receiver rotated. This suggests that the degree of rotational symmetry has a significant impact on omnidirectionality. Thus, the rest of the Platonic solids were excited under ultrasound to evaluate the effect of higher-order rotational symmetry (Figure 3a-e shows a detailed experimental setup). While the Platonic solid is expected to enhance the overall ultrasonic powering, electromechanical coupling, k_t, was somewhat lower than that of traditional piezoelectric material, PZT ($k_{t,BaTiO_3}$ = 0.5 vs $k_{t,PZT}$ = 0.72).[32,34] To compensate for such a material disadvantage, we revamped the ultrasonic powering scheme using focused ultrasound (FUS). FUS is currently used in the clinic for transcranial brain stimulation, providing an I_{SPTA} of 1−25 W/cm^2 over a highly focused area;[35−38] hence, it is compatible with our Platonic solid receivers. With the Platonic receiver placed at the focal zone of the FUS (7.5 cm for our case), 10-cycles of ultrasonic waves (duty cycle = 1.4%) were generated by 676.5 kHz sinusoidal signals (to match the resonant frequency) that are amplified through an RF amplifier (I_{SPTA} = 1.3 W/cm^2). The direction of the ultrasonic waves was fixed in the x-direction. Figure 3c shows an example of the input signal (top) and the received signal (bottom). The time delay ($\Delta t \sim 48$ μs) indicates the focal distance of 7.5 cm between the transducer and the receiver. Under the ultrasound field, the Platonic solids receivers were then rotated for a comprehensive study of angular misalignment sensitivity.

The voltage outputs seen at different axial angles confirmed that higher-order Platonic solids could enable omnidirectional ultrasonic powering; Figure 4 shows it in a polar coordinate system, and Supplementary Figure 4 displays it in a Cartesian coordinate system. As previously observed, the cubical receiver showed significant voltage losses at its vertices (45°, 135°, 225°, and 315°) that directly scattered the incoming ultrasonic waves. This resulted in an approximately 75% reduction in voltage output compared to its peak voltage ($V_{Cube,\ max}$ = 1.07 V, $V_{Cube,\ min}$ = 0.27 V) as shown in Figure 4a and

https://doi.org/10.1021/acsmaterialslett.3c00121
ACS Materials Lett. 2023, 5, 1876−1885

Table 3. Comparison of This Work to Other Ultrasonically Powered Implantable Medical Devices

Author	Year/Ref	Material	Form factor	Freq [MHz]	Tx [mm][a]	Rx [mm]	P_{Rx} [mW]	Depth [mm]	η [%]	Contribution
Song	2015/15	PZT	Cube	1.15	32.7 × 32.7 × 2	2 × 2 × 2	8.7	200	1.7	The first study on symmetric ultrasonic receivers for omnidirectional powering
			Rectangular	1.15	32.7 × 32.7 × 2	2 × 4 × 2	12.0		2.7	
			Rectangular	2.30	23.7 × 23.1 × 2	1 × 5 × 1	2.48		0.4	
Seo	2016 /6	PZT	Cube	1.85	6 mm OD	0.75 × 0.75 × 0.75	0.12	8.8	25	Ultrasound-mediated biopotential recording
Chang	2017/40	PMN−PT	Rectangular	0.95	0.55 × 0.55 × 0.4	0.9 × 0.9 × 0.5	0.125	85	-	The use of ultrasound for powering and communication for implantable devices
Charthad	2018/41	$BaTiO_3$	Rectangular	1.31	39 mm OD	1.65 × 1.65 × 1.5	3.0	105	0.04	Ultrasonically powered, electrical stimulation of peripheral nerves
Basaeri	2019/42	PZT−PMUT	Rectangular	0.08	12.8 mm OD	2 × 2 × 0.04	0.23	20−40	0.11−0.32	Angular and orientation misalignment sensitivity study in ultrasound for powering biomedical implants
Chang	2019/43	PMN−PT	Rectangular	0.97	32 elements	0.9 × 0.9 × 0.5	-	65	-	Ultrasound-mediated closed-loop multiaccess networking for implants
Shi	202117	PZT	Rectangular	8.3	192 elements, 0.2 × 0.2	0.3 × 0.3 × 0.267	0.8×10^{-6}	57	-	In vivo temperature monitoring using sub-1nW devices, powered by ultrasound
Gil	2021/21	PZT	Rectangular	0.4	-	3.5 × 6.5 × 1.5	0.01	50	-	Ultrasonically activated physiological monitoring system
Rong	2022/44	AlN-PMUT	Cube	3	-	Area: 2.55 mm^2 $t = 7.45\ \mu m$	0.042	25	0.236	Ultraminiaturized wireless power supply for implantable biomedical devices
Vo	2022/45	PZT	Rectangular	1.0	19 mm OD	1.08 × 1.08 × 1.44	0.4	-	-	Ultrasonically powered implants, in vivo study
Sayemul	2022/This work	$BaTiO_3$	Cube	0.67	44 mm OD	5.07 × 5.07 × 5.07	2.5	75	0.73	3D printed Platonic solids as a lead-free piezoelectric receiver; Omnidirectional ultrasonic powering
			Sphere			3.5 (radius)	6.7		1.95	
			Octahedron			6.67 (edge)	6.8		1.98	
			Dodecahedron			2.73 (edge)	16.8		4.9	

[a]"OD" indicates the Outer Diameter. For other transmitter shapes dimension is written as height × width × thickness in the millimeter (mm) unit.

https://doi.org/10.1021/acsmaterialslett.3c00121
ACS Materials Lett. 2023, 5, 1876−1885

Supplementary Figure 4a-b. Although the octahedron showed similar behavior at every vertex, it generated the peak voltage every 30° due to its higher periodicity, as shown in Figure 4b and Supplementary Figure 4c. The polar plot was created by repeating the measurement up to 140° since the wire connection was made to one of the faces of the octahedron. The max voltage reduction was slightly less, at 68% of the peak voltage ($V_{Octahedron,\ max}$ = 2.22 V, $V_{Octahedron,\ min}$ = 0.71 V). This evidently validated that higher-order Platonic solids improved the angular response. As expected, the dodecahedron that has 12 faces with symmetry every 18° showed even more prominent improvement with almost consistent voltage outputs throughout all axial rotations ($V_{Dodecahedron,\ max}$ = 4.17 V, $V_{Dodecahedron,\ min}$ = 2.95 V voltage output reduction of 29%), as shown in Figure 4c and Supplementary Figure 4d. Lastly, the sphere is shown in Figure 4d and Supplementary Figure 4e, demonstrated near omnidirectional powering. However, the overall voltage output itself was not significantly comparable to the Platinic solids ($V_{Sphere,\ max}$ = 2.11 V). It is attributed to the curved surface that may have grazed off the incoming ultrasonic waves. The measured minimum voltage output ($V_{Sphere,\ min}$) was 1.53 V for the spherical receiver, which is 27% less than the maximum voltage output, likely due to imperfections in the fabrication.

The above results conclude that the radially poled dodecahedron was capable of delivering the highest power output with excellent omnidirectional responses. Other spatial characterizations for radially poled Platonic solids were also conducted. The operation depth was determined by the FUS transducer, which was from 5 to 13 cm from the transducer (Supplementary Figure 5a). The overall voltage outputs were proportional to the input acoustic intensity, shown in Supplementary Figure 5b. When the regular ultrasound was used, the output was only 20% of the FUS; however, it extended the operational depth up to 30 cm as shown in Supplementary Figure 5c. The use of regular ultrasound could also cover slightly better for the offset misalignment (off from the center of the external ultrasound transducer) but only by a couple of centimeters (Supplementary Figure 5d).

Lastly, the IV (current–voltage) characteristics (Figure 4e), power density (Figure 4f), and power transfer efficiency of the Platonic solid receivers were investigated with variable load resistances. As anticipated, the dodecahedron could produce the highest output power ($P_{out,\ Dodecahedron}$ = 16.8 mW; η = 4.90%); $P_{out,\ Octahedron}$ = 6.8 mW (η = 1.98%), $P_{out,\ Cube}$ = 2.5 mW (η = 0.73%), and $P_{out,\ Sphere}$ = 6.7 mW (η = 1.95%). These electrical power levels were optimized with a load resistance of 200–400 Ω. It is noteworthy that the Platonic solids receivers were operated at their corresponding resonance frequencies, leaving a source impedance to be mostly resistive.[15,39] Although the power transfer efficiencies (η) were relatively low, considering the small receiver dimensions and longer distance in power transfer, the results outperformed traditional inductive powering.[24] Note that the radially poled Platonic solids ($C_{Axial,\ average}$ = 22.26 pF) showed a 10-fold increase in capacitance compared to that of axially poled ones ($C_{Radial,\ average}$ = 272.21 pF), measured with an impedance analyzer (E5061B, Keysight). As the higher capacitance can reduce the overall power efficiency, further refinement using impedance matching will be necessary.[15] Considering the millimeter scale, omnidirectional, and lead-free, the reported radially poled Platonic solids piezoelectric receiver by far outperformed our previous results or other ultrasonic-powered biomedical devices (Table 3). For example, the radially poled dodecahedron receiver could easily generate 107.76 mW/cm^3, which is significantly higher than our previous work of ultrasonic powering using diced PZT slabs that showed 13.3 mW/cm^3.[15]

Thus far, radially poled, highly symmetric Platonic solids have shown drastic improvements in ultrasonic powering in terms of omnidirectionality and superior power output. Now, we discuss seamless packaging using the radially poled Platonic solid ultrasonic receiver. This packaging method has the potential to address the outstanding challenges of powering and packaging in developing implantable devices. To this end, we utilized the cylindrical void space of the radially poled Platonic solid, which was utilized during poling process, to contain circuitry. This allows the Platonic solid receivers to serve not only as a power source for small implants but also as a packaging shell. In this sense, $BaTiO_3$ material is especially suitable due to its excellent biocompatibility.[33,46] Lastly, the 3D printability presented in our work allows for customizing the dimensions of the Platonic solid packaging. For energy storage purposes, piezoelectric energy harvesting circuitry paired with a supercapacitor can be used. Furthermore, frequent charging operations (e.g., once daily) can warrant full potential; the time interval between external ultrasound charging, operation duration, and discharge interval can be tailored based on system and therapeutic requirements.

As a proof-of-concept, we created a Platonic solid-packaged implantable light source (*μLight*), which we had previously reported for photodynamic therapy in deeply seated tumors.[19] An LED and a rectifier circuit are placed inside the cylindrical void (2 mm in diameter and height). The *μLight* source could fit into a 10-gauge biopsy needle (diameter = 3.4 mm), which allowed for minimally invasive implantation. The *μLight* was tested *ex vivo* using porcine tissue (Figure 5a-b). After creating

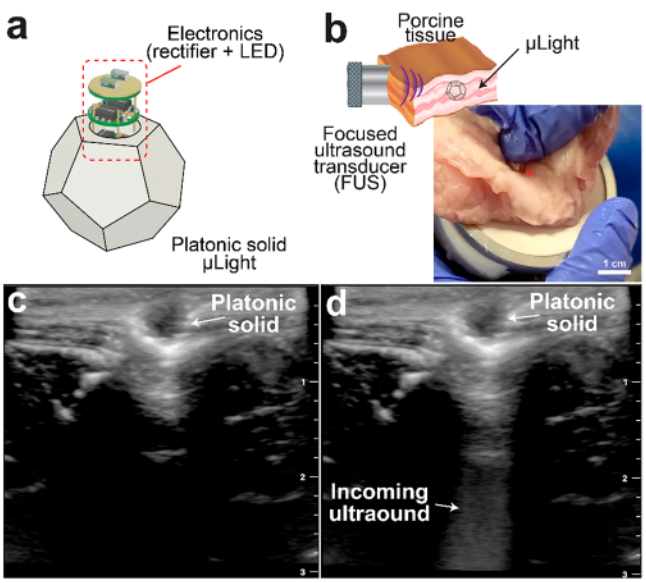

Figure 5. Implantable light source (*μLight*) using Platonic solid receiver: (a) a LED and rectifier circuit are embedded in the concentric void of the Platonic solid receiver. (b) Ex vivo experiment shows visible red light through the porcine tissue from Platonic solid. (c) Ultrasonic imaging is shown after the implantation and (d) during operation (incoming ultrasonic waves can be seen in the imaging).

https://doi.org/10.1021/acsmaterialslett.3c00121
ACS Materials Lett. 2023, 5, 1876–1885

a small hole in porcine tissue, the *μLight* was implanted by pushing it into the hole until it reached the focal point of the FUS, while being monitored by the ultrasonic imaging system (Figure 5c-d) (iQ+, Butterfly Network). We delivered the FUS waves in a bursting mode, i.e., 10 cycles of 676.5 kHz sinusoidal waves (I_{SPTA} = 15 mW/cm^2). Visible LED illumination through porcine tissue was clearly observed (Figure 5b). The *μLight* was able to deliver light consistently even when it was not aligned in a specific direction, demonstrating omnidirectional operation enabled by the radially poled Platonic solids.

In conclusion, we reported a new class of ultrasonic receivers as a prerequisite for omnidirectional powering based on Platonic solids design and realized using 3D printable barium titanate material. It could serve as a translational solution for a variety of implanted devices. We investigated an omnidirectional ultrasonic receiver using radial poling and extremely symmetric transducer designs. Our research demonstrated how symmetrical Platonic solids could expand the effective receiving area of ultrasonic waves coming from any random angle. We observed superior power transfer efficiency with true omnidirectionality when the Platonic solids were poled in a radial direction. Moreover, the Platonic solids were also demonstrated as packaging shells, enabling seamless packaging of circuitry. Combined, the Platonic solids offer a versatile and dual-function solution as a relatable power source and seamless packaging for IMDs.

■ EXPERIMENTAL SECTION

3D Fabrication of the Barium Titanate Platonic Receiver. The detailed fabrication process is shown in Supplementary Figure 6. The binder solution was prepared first by dissolving polyvinyl fluoride (PVDF; Alfa Aesar) into *N*,*N*′-dimethylformamide (DMF; Thermo Scientific) at a 1:8.8 weight ratio in a heated water bath (temperature = 80 °C) (Supplementary Figure 6a). Then, $BaTiO_3$ nanoparticles (500 nm; US research nanomaterials) were slowly added to the binder solution until the weight ratio reached 3.345:1 of $BaTiO_3$:PVDF/DMF (Supplementary Figure 6b). Any clumps that may have been created were removed by stirring the mixture continuously. The mixture was then infused into a printing syringe (10 mL volume and 600 μm nozzle) for 3D printing of the Platonic solids (Supplementary Figure 6c). After 3D printing, residual DMF on the surfaces was removed by soft-baking at 120 °C in an oven (AccuTemp-09, Across Intl.) (Supplementary Figure 6d). A concentric void was made on one face of each group of Platonic solids in order to explore the impact of poling direction, particularly radial poling. The circuitry can be packaged invisibly in this concentric cylindrical vacuum, offering seamless packaging. After that, the platonic solids underwent a two-step postprocessing procedure called sintering and debinding (Supplementary Figure 6e). The debinding process thermally removed the remaining binder additives (i.e., PVDF and DMF). Then, the sintering process fused the $BaTiO_3$ nanoparticles to form the bulk piezoelectric Platonic solid. They were done in sequence in a tube furnace (GSL-1600X, MTI Corp.). The debinding process was performed for 1 h at 650 °C (ramp = 5 °C/min), followed by the sintering process for 3 h at 1,125 °C (ramp = 5 °C/min). After the sintering process, poling was performed to align the randomly oriented electric dipoles (Supplementary Figure 6f). For radially poled samples, a thin layer of silver epoxy (8331, MG Chemical) was applied throughout the outer surface of the Platonic solids as one electrode and inside the concentric void as another electrode. For axially poled samples, the electrodes were created on opposite-faced surfaces (a 1 mm gap separated the electrodes for the sphere). The poling stage was custom-made using a copper plate and a spring-loaded metallic needle affixed to the top. The electrode sides of the Platonic solids were then sandwiched. The Platonic solids in the poling stage were then submerged in a heated silicone oil bath (120 °C, i.e., curie temperature); silicone oil helped with preventing the risk of electrical conductions through the ionized air gap during poling. A high electric field (>1.0 kV/mm; a high-voltage DC supply (230−30R, Spellman) was applied across the Platonic solids for 2 h. Lastly, an assembled rectifier circuit and an LED were placed inside the radially poled Platonic solids (Supplementary Figure 6g). A droplet of biocompatible epoxy glue was added to the void for secure packaging.

Ultrasonic Powering Setup. The resonance frequency experiment setup is shown in Figure 3a. A sinusoid electrical signal (100 kHz−1 MHz) from a signal generator via a wide band RF amplifier (1040L, ENI Inc.) was applied as input excitation to the Platonic solids. The output, in terms of acoustic waves, emitted from the Platonic solids was captured using a fiber optic needle hydrophone (FOH-64, Precision Acoustics). The experimental setups for the orientation misalignment study, operation depth, offset from the transmitter, and input intensity response are shown in Figure 3b and Figure 3d,e. Two different ultrasonic transducers were used as transmitters: 1) a focused ultrasonic transducer (TXH-0.67−75, Precision Acoustics), and 2) a planner ultrasonic transducer (TXH-500−45, Precision Acoustics). The experiment was performed in a distilled water tank to mimic the acoustic impedance of soft tissue, which is around 1.5 MRayl. The Platonic solids were then affixed to a shaft and placed underwater at the end of a near field, or focal distance, from the ultrasonic transmitters. A custom XY manipulator (Makeblock) allowed us to move the Platonic solids at various distances to measure the operational depth, offset, and acoustic intensity responses. We intentionally omitted the offset study in the *Z*-direction because it is expected to be similar to the offset in the *Y*-direction. For the rotational measurements in the orientation misalignment study, another custom-made rotational platform was used (Figure 3e), which had a 1° step resolution.

Finite Element Analysis. The resonance frequencies were verified using 3D finite element analysis in the frequency domain from 100 kHz to 1 MHz using COMSOL Multiphysics software (ver. 5.2). The results are shown in Supplementary Figure 3. A CAD software (Fusion 360, Autodesk) was used for drawing the 3D models, and then they were imported into the COMSOL software. The material properties for both axial poling and radial poling simulations were taken for piezoelectric $BaTiO_3$ in the software environment. A solid mechanics module was used for simulating and computing the stress distribution in the Platonic solids due to incident pressure (206.6 kPa, the same pressure we measured from the experiments with acoustic waves underwater). Then, the electric displacement field and potential distribution were calculated using an electrostatic interface module in the COMSOL software.

https://doi.org/10.1021/acsmaterialslett.3c00121
ACS Materials Lett. 2023, 5, 1876−1885

■ ASSOCIATED CONTENT

Supporting Information

The Supporting Information is available free of charge at https://pubs.acs.org/doi/10.1021/acsmaterialslett.3c00121.

1) The Periodicity of Platonic solids, 2) the Theoretical calculation of the angular response of radially poled Platonic solid receivers study, 3) the COMSOL simulation, 4) the Orientation misalignment response, and 5) the Spatial characterization of Platonic solids under ultrasound (PDF)

■ AUTHOR INFORMATION

Corresponding Authors

Albert Kim − *Department of Medical Engineering, University of South Florida, Tampa, Florida 33620, United States;* orcid.org/0000-0003-1539-1246; Email: akim1@usf.edu

Seunghyun Song − *Department of Electronics, Sookmyung Women's University, Seoul 04310, Korea;* orcid.org/0000-0002-6181-4660; Email: shsong.ee@sookmyung.ac.kr

Won Seok Chang − *Department of Neurosurgery, Yonsei University College of Medicine, Seoul 03722, Korea;* Email: changws@yonsei.ac.kr

Authors

Sayemul Islam − *Department of Medical Engineering, University of South Florida, Tampa, Florida 33620, United States;* orcid.org/0000-0001-6062-1974

Eungyoul Oh − *Department of Electronics, Sookmyung Women's University, Seoul 04310, Korea*

Chaerin Jun − *Department of Electronics, Sookmyung Women's University, Seoul 04310, Korea*

Jungkwun Kim − *Department of Electrical Engineering, University of North Texas, Denton, Texas 76203, United States*

Complete contact information is available at: https://pubs.acs.org/10.1021/acsmaterialslett.3c00121

Author Contributions

A.K. and S.H.S. initiated the project. S.I. fabricated and tested the transducers. E.O., C.J, W.S.C., and S.H.S. performed theoretical analyses. S.I. and J.K. performed the simulation. S.I., E.O., W.S.C., S.H.S., and A.K. performed data analysis. A.K. and S.I. created all figures. A.K., S.H.S., and W.S.C. led the preparation of the manuscript and contributed to the editorial modification of the overall text. CRediT: **Sayemul Islam** formal analysis, investigation, software, visualization, writing-original draft; **Eungyoul Oh** formal analysis, validation, visualization; **Chaerin Jun** formal analysis, validation; **Jungkwun Kim** funding acquisition, software, writing-review & editing; **Won Seok Chang** formal analysis, funding acquisition, writing-review & editing; **Seunghyun Song** conceptualization, formal analysis, funding acquisition, investigation, methodology, supervision, validation, writing-original draft, writing-review & editing; **Albert Kim** conceptualization, formal analysis, funding acquisition, investigation, methodology, project administration, resources, supervision, validation, visualization, writing-original draft, writing-review & editing.

Notes

The authors declare the following competing financial interest(s): Albert Kim and Seunghyun Song are inventors on US Provisional Application No. 63/383,207 (filed on November 10, 2022).

■ ACKNOWLEDGMENTS

The authors would like to thank Dr. Steven M. Chemtob and Dr. Michael J. Zdilla at the Department of Chemistry, Temple University for their help with the XRD measurements. We also thank Michael Domic and Long Zhu for their help with the experiments, and M. Park for initial pilot experiments. This work is supported by the NSF CAREER award (ECCS-2245090), NSF ECCS-2300985, NSF CNS-2245090, NSF ECCS-2245092, and NSF ECCS-2306330. S.H.S., E.O., and C.J. acknowledge the support from the National Research Foundation of Korea (NRF) grant funded by the Korean government (MSIT; No. 2020R1C1C1006671).

■ REFERENCES

(1) Greatbatch, W. Medical Cardiac Pacemaker. U.S. Patent US3057356A, July 22, 1960.

(2) Chardack, W. M.; Gage, A. A.; Greatbatch, W. A transistorized, self-contained, implantable pacemaker for the long-term correction of complete heart block. *Surgery* **1960**, *48*, 643−654.

(3) Mackay, R. S.; Jacobson, B. Endoradiosonde. *Nature* **1957**, *179*, 1239−1240.

(4) House, W. F. Cochlear implants. *Ann. Otol Rhinol Laryngol* **1976**, *85*, 1−93.

(5) Rogers, J. A.; Someya, T.; Huang, Y. Materials and mechanics for stretchable electronics. *Science* **2010**, *327*, 1603−1607.

(6) Seo, D.; et al. Wireless Recording in the Peripheral Nervous System with Ultrasonic Neural Dust. *Neuron* **2016**, *91*, 529−539.

(7) Han, J. J. The Aveir Leadless Pacing System receives FDA approval. *Artif. Organs* **2022**, *46*, 1219−1220.

(8) Musk, E.; Neuralink. An Integrated Brain-Machine Interface Platform With Thousands of Channels. *J. Med. Internet Res.* **2019**, *21*, No. e16194.

(9) Scrosati, B.; Abraham, K. M.; Schalkwijk, W. A. v.; Hassoun, J. *Lithium batteries: advanced technologies and applications*; Wiley, 2013.

(10) Van Schuylenbergh, K.; Puers, R. *Inductive Powering*; Springer Dordrecht, 2009. DOI: 10.1007/978-90-481-2412-1.

(11) Greatbatch, W.; Lee, J. H.; Mathias, W.; Eldridge, M.; Moser, J. R.; Schneider, A. A. The solid-state lithium battery: a new improved chemical power source for implantable cardiac pacemakers. *IEEE Trans Biomed Eng.* **1971**, *BME-18*, 317−324.

(12) Holmes, C. F. The bourner lecture: Electrochemical power sources — an important contributor to modern health care. *J. Power Sources* **1997**, *65*, xv−xx.

(13) *Nucleus 24 Cochlear Implant System*; U. S. Food and Drug Administration, 2022.

(14) Zhang, J.; et al. Smart soft contact lenses for continuous 24-h monitoring of intraocular pressure in glaucoma care. *Nat. Commun.* **2022**, *13*, 5518.

(15) Song, S. H.; Kim, A.; Ziaie, B. Omnidirectional Ultrasonic Powering for Millimeter-Scale Implantable Devices. *IEEE Trans Biomed Eng.* **2015**, *62*, 2717−2723.

(16) Sonmezoglu, S.; Fineman, J. R.; Maltepe, E.; Maharbiz, M. M. Monitoring deep-tissue oxygenation with a millimeter-scale ultrasonic implant. *Nat. Biotechnol.* **2021**, *39*, 855−864.

(17) Shi, C.; et al. Application of a sub-0.1-mm(3) implantable mote for in vivo real-time wireless temperature sensing. *Sci. Adv.* **2021**, *7*, 1−10.

(18) Campbell, R.; Shim, H.; Choi, J.; Park, M.; Byun, E.; Islam, S.; Song, S. H.; Kim, A. Implantable Cisplatin Synthesis Microdevice for Regional Chemotherapy. *Adv. Healthcare Mater.* **2021**, *10*, 2001582.

(19) Kim, A.; et al. An Implantable Ultrasonically-Powered Micro-Light-Source (microLight) for Photodynamic Therapy. *Sci. Rep* **2019**, *9*, 1395.

(20) Maleki, T.; et al. An ultrasonically powered implantable micro-oxygen generator (IMOG). *IEEE Trans Biomed Eng.* **2011**, *58*, 3104–3111.
(21) Gil, B.; Anastasova, S.; Yang, G. Z. Low-powered implantable devices activated by ultrasonic energy transfer for physiological monitoring in soft tissue via functionalized electrochemical electrodes. *Biosens. Bioelectron.* **2021**, *182*, 113175–113175.
(22) Charthad, J.; et al. A mm-Sized Wireless Implantable Device for Electrical Stimulation of Peripheral Nerves. *IEEE Transactions on Biomedical Circuits and Systems* **2018**, *12*, 257–270.
(23) Shi, C. Application of a sub-0.1-mm(3) implantable mote for in vivo real-time wireless temperature sensing. *Sci. Adv.* **2021**, *7*, eabf6312.
(24) Denisov, A.; Yeatman, E. Ultrasonic vs. Inductive Power Delivery for Miniature Biomedical Implants. *2010 International Conference on Body Sensor Networks*, 2010, 84–89. DOI: 10.1109/bsn.2010.27.
(25) Kim, A.; Powell, C. R.; Ziaie, B. An implantable pressure sensing system with electromechanical interrogation scheme. *IEEE Transactions on Biomedical Engineering* **2014**, *61*, 2209–2217.
(26) Kim, H. E.; Islam, S.; Park, M.; Kim, A.; Hwang, G. A Comprehensive Analysis of Near-Contact Photobiomodulation Therapy in the Host-Bacteria Interaction Model Using 3D-Printed Modular LED Platform. *Advanced Biosystems* **2020**, *4*, 1900227.
(27) Park, S. J.; et al. Phototactic guidance of a tissue-engineered soft-robotic ray. *Science* **2016**, *353*, 158–162.
(28) Yates, R. C.; Steinhaus, H. Mathematical Snapshots by H. Steinhaus. *National Mathematics Magazine* **1939**, *13*, 351–352.
(29) Frey, M. H.; Payne, D. A. Grain-size effect on structure and phase transformations for barium titanate. *Phys. Rev. B* **1996**, *54*, 3158–3168.
(30) Berlincourt, D.; Jaffe, H. Elastic and Piezoelectric Coefficients of Single-Crystal Barium Titanate. *Phys. Rev.* **1958**, *111*, 143–148.
(31) Park, M.; et al. Human Oral Motion-Powered Smart Dental Implant (SDI) for In Situ Ambulatory Photo-biomodulation Therapy. *Adv. Healthcare Mater.* **2020**, *9*, 2000658–2000658.
(32) Roberts, S. Dielectric and Piezoelectric Properties of Barium Titanate. *Phys. Rev.* **1947**, *71*, 890–895.
(33) Acosta, M.; et al. BaTiO3-based piezoelectrics: Fundamentals, current status, and perspectives. *Applied Physics Reviews* **2017**, *4*, 041305–041305.
(34) Jaffe, H. Piezoelectric Ceramics. *J. Am. Ceram. Soc.* **1958**, *41*, 494–498.
(35) Legon, W.; et al. Transcranial focused ultrasound modulates the activity of primary somatosensory cortex in humans. *Nature Neuroscience* **2014**, *17*, 322–329.
(36) Tufail, Y.; et al. Transcranial pulsed ultrasound stimulates intact brain circuits. *Neuron* **2010**, *66*, 681–694.
(37) Deffieux, T.; et al. Low-Intensity Focused Ultrasound Modulates Monkey Visuomotor Behavior. *Curr. Biol.* **2013**, *23*, 2430–2433.
(38) Bystritsky, A.; et al. A review of low-intensity focused ultrasound pulsation. *Brain Stimulation* **2011**, *4*, 125–136.
(39) Vives, A. A. *Piezoelectric Transducers and Applications*; Springer, 2008. DOI: 10.1007/978-3-540-77508-9.
(40) Chang, T. C.; Wang, M. L.; Charthad, J.; Weber, M. J.; Arbabian, A. A 30.5mm3 fully packaged implantable device with duplex ultrasonic data and power links achieving 95kb/s with < 10–4 BER at 8.5 cm depth. *Digest of Technical Papers - IEEE International Solid-State Circuits Conference* **2017**, *60*, 460–461.
(41) Charthad, J.; et al. A mm-Sized Wireless Implantable Device for Electrical Stimulation of Peripheral Nerves. *IEEE Trans Biomed Circuits Syst* **2018**, *12*, 257–270.
(42) Basaeri, H.; Yu, Y.; Young, D.; Roundy, S. Acoustic power transfer for biomedical implants using piezoelectric receivers: effects of misalignment and misorientation. *Journal of Micromechanics and Microengineering* **2019**, *29*, 084004.
(43) Chang, T. C.; Wang, M.; Arbabian, A. Multi-Access Networking with Wireless Ultrasound-Powered Implants. *BioCAS 2019 - Biomedical Circuits and Systems Conference, Proceedings*, 2019, 1–4. DOI: 10.1109/BIOCAS.2019.8919144.
(44) Rong, Z.; Zhang, M.; Ning, Y.; Pang, W. An ultrasound-induced wireless power supply based on AlN piezoelectric micromachined ultrasonic transducers. *Sci. Rep* **2022**, *12*, 16174.
(45) Vo, J.; et al. Assessment of miniaturized ultrasound-powered implants: an in vivo study. *J. Neural Eng.* **2020**, *17*, 016072.
(46) Luo, C.; et al. A Flexible Lead-Free BaTiO3/PDMS/C Composite Nanogenerator as a Piezoelectric Energy Harvester. *Energy Technology* **2018**, *6*, 922–927.

https://doi.org/10.1021/acsmaterialslett.3c00121
ACS Materials Lett. 2023, 5, 1876–1885